Intrazeolite Nonstoichiometric Tungsten Oxides $n[WO_{3-x}]$-$Na_{56}Y$ ($0 < n \leq 32$, $0 \leq x \leq 1$)

Geoffrey A. Ozin,*,† Richard A. Prokopowicz,† and Saim Özkar‡

Contribution from the Advanced Zeolite Materials Science Group, Lash Miller Chemistry Laboratories, University of Toronto, 80 St. George Street, Toronto, Ontario, Canada M5S 1A1, and the Chemistry Department, Middle East Technical University, 06531 Ankara, Turkey.
Received February 19, 1992

Abstract: The photooxidation of α-cage encapsulated $n[W(CO)_6]$-$Na_{56}Y$, where $0 < n \leq 16$ and $Na_{56}Y$ denotes sodium zeolite Y, provides a mild, clean, and quantitative synthetic pathway to molecular dimension tungsten(VI) oxide moieties, encapsulated within the void structure of the zeolite Y host, according to the reaction stoichiometry

$$n[W(CO)_6]\text{-}Na_{56}Y + {}^9/_2 nO_2 \xrightarrow{h\nu} n[WO_3]\text{-}Na_{56}Y + 6nCO_2$$

Following photooxidation, half of the α-cage void volume in the $Na_{56}Y$ host is freed so that subsequent precursor (saturation level) impregnations/photooxidations can be carried out in a stepwise fashion, proceeding as n = 16, 24, 28, 30, ..., 32 per unit cell. Thermal vacuum treatment of these materials proceeds in two well-defined steps around 300 and 400 °C to yield encapsulated $n[WO_{3-x}]$-$Na_{56}Y$ materials having x = 0.5 and 1, respectively. This reduction process is reversible by heating in an O_2 atmosphere at 300 °C. The entire redox process can be summarized according to the reaction stoichiometry

$$n[WO_3]\text{-}Na_{56}Y \xrightarrow[\text{vacuum}]{300\,^\circ C} n[WO_{2.5}]\text{-}Na_{56}Y \xrightarrow[\text{vacuum}]{400\,^\circ C} n[WO_2]\text{-}Na_{56}Y$$

$$\xleftarrow[O_2]{300\,^\circ C}$$

The combined results of a multiprong analysis (PXRD, STEM-EDX, TEM, EXAFS, XPS, EPR, ^{29}Si MAS-NMR, ^{23}Na DOR-NMR, UV-vis, gravimetry) of the aforementioned materials indicate that in $Na_{56}Y$ and at loading levels of 16 molecules per unit cell (one per α-cage) WO_3 and $WO_{2.5}$ moieties are found exclusively as μ-dioxo- and μ-oxo-bridged dimers, that is W_2O_6 and W_2O_5, respectively. These are each anchored through terminal oxotungsten bonds to two of the four site II Na^+ cations located in an α-cage, denoted $(ZONa)...O_2W^{6+}(\mu\text{-}O)_2W^{6+}O_2...(NaOZ)$ and $(ZONa)...O_2W^{5+}(\mu\text{-}O)W^{5+}O_2...(NaOZ)$. For WO_3, this dimer structure is maintained at loading levels of 28 molecules per unit cell and up to a fully loaded 32 (two per α-cage) sample. In the case of $WO_{2.5}$, the spin-paired dimers that are formed at the 16 loading level assume a spin-paired W_4O_{10} tetrameric structure at 32 molecules per unit cell, denoted $(ZONa)_2...O_4W_2^{5+}(\mu\text{-}O)_2W_2^{5+}O_4...(NaOZ)_2$. The tetramer is anchored via terminal oxotungsten bonds to all four site II Na^+ cations in an α-cage. At loading levels of 16, 28, and 32 molecules per unit cell, the WO_2 species are consistently monomeric with a structure described in terms of a *cis*-dioxotungsten(IV) moiety having a primary anchoring interaction to two framework oxygens most likely part of an α-cage oxygen 4-ring, as well as a secondary interaction involving an oxotungsten bond and a site II Na^+ cation denoted $(ZO)_2...W^{4+}O_2...(NaOZ)_2$. Intrazeolite topotactic chemistry of the above type provides access to a new class of $n[WO_{3-x}]$-$Na_{56}Y$ materials in which the oxygen content and structural and electronic properties of the encapsulated tungsten oxide units can be conveniently fine tuned. In this way one can precisely control the oxidation state, extent of electron injection (n-doping), and degree of band filling of an intrazeolte tungsten(VI) oxide supralattice (miniband description).

Introduction

WO_3 and WO_2 are the simplest oxides of tungsten. The stable lemon yellow form of WO_3 has a slightly distorted cubic ReO_3 structure in which octahedral WO_6 building blocks share every corner, but no edges, with neighboring WO_6 units.[1] A very disorted rutile type structure exists for WO_2 with strong 2.49 Å W-W bonds.[1] Thermal treatment of WO_3 induces loss of oxygen from the lattice to produce a range of nonstoichiometric oxides WO_{3-x} with the composition range $0 \leq x \leq 1$. One class of these materials is the Magnêli crystallographic shear structure type.[2] The structural principle upon which these are built involves the systematic replacement of corner-only sharing WO_6 units in the parent WO_3 structure by edge sharing ones, yielding phases of composition W_nO_{3n-1}, W_nO_{3n-2}, and the like. WO_3 itself is an allowed, indirect band gap semiconductor[3] (E_g = 2.7 eV). It has an impressive range of solid-state applications, including the following: selective hydrocarbon oxidation catalysis; rechargeable solid-state batteries; electrochromic devices, mirrors, and displays; pH-sensitive microelectrochemical transistors and chemical sensors; and semiconductor liquid-junction solar and electrochemical cells.[4]

Recently we reported[5] some details of the preparation and partial characterization of a new form of tungsten(VI) oxide. This involved the photolytic synthesis of intrazeolite $n[WO_3]$-$Na_{56}Y$ in the composition range $0 < n \leq 32$, from the $n[W(CO)_6]$-$Na_{56}Y$ precursor. The encapsulated tungsten(VI) oxide guests were subsequently established to be single size and shape W_2O_6 dimer units housed in the diamond network of α-cages of the $Na_{56}Y$ host lattice.[6] These could be arranged to grow in population and were shown from an EXAFS structure analysis[7] to form a supralattice of dimers at half-loading n = 16. Above this filling, only the population of W_2O_6 dimers was found to increase up to the highest loading value of n = 28 studied by EXAFS at that time.[7]

In this paper we extend this study and show that the trend continues up to a saturation loading of n = 32, to yield a supralattice of dimers-of-dimers rather than tetramers. Particularly exciting is the additional discovery that the oxygen content of these dimers can be quantitatively adjusted by means of a thermal

* To whom correspondence should be sent.
† University of Toronto.
‡ Middle East Technical University.

(1) Cotton, F. A.; Wilkinson, G. *Advanced Inorganic Chemistry*, 5th ed.; John Wiley & Sons: New York, 1988.
(2) Adams, D. M. *Inorganic Solids*; Wiley & Sons: London, 1979. West, A. R. *Solid State Chemistry and its Applications*; Wiley & Sons: Chichester, 1984 (and references cited therein).
(3) Nanthakumar, A.; Armstrong, N. R. In *Semiconductor Electrodes*; Finklea, H. O., Ed.; Elsevier Publ. Co.: Amsterdam, 1988 (and references cited therein).
(4) Rao, C. N. R.; Gopalakrishnan, J. *New Directions in Solid State Chemistry*; Cambridge University Press: Cambridge, 1986.
(5) Ozin, G. A.; Özkar, S. *J. Phys. Chem.* **1990**, *94*, 7556.
(6) Ozin, G. A.; Özkar, S.; Macdonald, P. M. *J. Phys. Chem.* **1990**, *94*, 6939.
(7) Moller, K.; Bein, T.; Özkar, S.; Ozin, G. A. *J. Phys. Chem.* **1991**, *95*, 5276.

0002-7863/92/1514-8953$03.00/0

Chart I

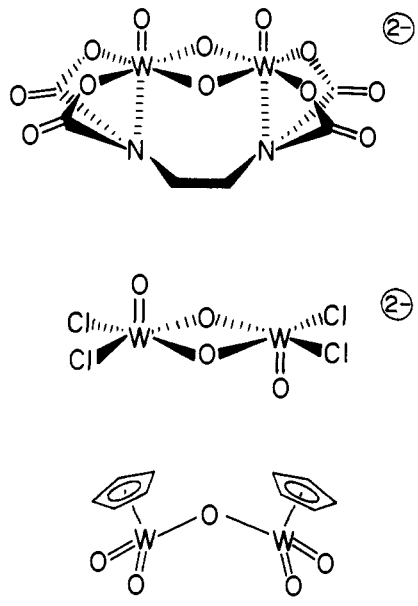

vacuum induced reversible reductive-elimination oxidative-addition sequence of reactions involving dioxygen. (A brief conference report[8] of this work has appeared.) This provides access to a new class of $n[WO_{3-x}]$–$Na_{56}Y$ materials covering the composition range $0 < n \leq 32$ and $0 \leq x \leq 1$, in which the oxygen content and structural and electronic properties of the encapsulated W_2O_6 dimers are changed. By this means, one can systematically manipulate the oxidation state, electronic coupling, degree of n-doping, and extent of "miniband filling" of an intrazeolite tungsten(VI) oxide supralattice. A primary goal of this study is to elucidate the exact nature of the encapsulated tungsten oxide guests in the nonstoichiometric group of materials $n[WO_{3-x}]$–$Na_{56}Y$ over the full composition range of $0 < n \leq 32$ and $0 \leq x \leq 1$.

Experimental Section

The high-purity crystalline sodium zeolite Y having the unit cell composition $Na_{56}(AlO_2)_{56}(SiO_2)_{136}\cdot xH_2O$ was obtained from Dr. Edith Flanigen at Union Carbide, Tarrytown, NY. In order to remove cation defect sites, thermally dehydrated/calcined $Na_{56}Y$ was slurried with 0.01 M NaCl, 0.01 M NaOH solution and washed until free of Cl^-. $(NH_4)_{56}Y$ and $H_{56}Y$ were prepared by the use of standard ion exchange techniques and deammination procedures.[9] All zeolite samples were stored over saturated NH_4Cl solution to ensure constant humidity until use. The $W(CO)_6$ was purchased from Strem Chemicals Inc., Newbury-Port, Ma.

The precursor samples denoted $n[W(CO)_6]$–$Na_{56}Y$ and the photooxidation products denoted $n[WO_{3-x}]$–$Na_{56}Y$ were prepared according to the procedures[5,10] described previously, using specially designed cells[11] for complete in situ treatments. The thermal reductive-elimination and oxidative-addition of oxygen, for the interconversion of $n[WO_3]$–$Na_{56}Y$, $n[WO_{2.5}]$–$Na_{56}Y$, and $n[WO_2]$–$Na_{56}Y$, were carried out in the cells at 300 and 400 °C in dynamic vacuum and 600 Torr of O_2, respectively.

The gravimetric analyses were performed in a specially designed cell which basically consists of a quartz tube (25 mm in diameter and 12 cm in length) and a greaseless stopcock allowing for the $W(CO)_6$ sample to be admitted or a vacuum applied. After in situ dehydration and calcination,[10] the zeolite sample is exposed to the $W(CO)_6$ vapor under dynamic vacuum. The increase in mass is determined in an analytical balance. Exposure to the $W(CO)_6$ vapor was continued gradually until no further increase in the mass of the zeolite sample was observed. The sample was then irradiated in the presence of oxygen gas, using a 450 W high-pressure xenon arc lamp (OSRAM XBO), a 10-cm water cell IR filter, and a $\lambda < 345$ nm optical cut-off filter. After the gases (O_2 and CO_2) were pumped out at room temperature, the sample was heated under vacuum for 1 h at 300 °C to produce $n[WO_{2.5}]$–$Na_{56}Y$ and for 1 h at 400 °C for the further reduction to $n[WO_2]$–$Na_{56}Y$. The changes in mass were recorded at every stage and used for the stoichiometric determinations.

Elemental analyses for Na, Al, and W were performed by Neutron Activation Analysis on the University of Toronto slowpoke reactor.

Optical reflectance spectra were obtained on a Perkin-Elmer 330 instrument using a $BaSO_4$ disk as a reference. Powder XRD patterns were recorded on a Philips PW 1051/Scintag PADX θ–θ diffractometer using Ni-filtered Cu Kα radiation (1.54178 Å). ^{29}Si, ^{27}Al, and ^{23}Na MAS-NMR spectra of solid samples were recorded on a Chemagnetics CMX-300 instrument. ^{23}Na DOR-NMR spectra were recorded at 11.7 T magnetic field on a Chemagnetics CMX-500 using a probe built at Berkely[22] and described elsewhere.[23] Solid state EPR data were collected on a Bruker ESP-300 spectrometer. XPS measurements were performed at the University of Western Ontario Surface Science Facility using an SSX-100 system which utilized monochromatic Al Kα X-rays capable of being focused to a spot size of 150 μm and a pass energy of 50 eV. Binding energies have been corrected for sample charging effects by referencing all peaks to the C(1s) peak corresponding to the adventitious carbon component which was assigned the value[12] of 284.9 eV. Differential charging effects were compensated using a conductive mesh-electron flood gun technique,[13] and were thus reduced to yield C(1s) line widths of 1.5 eV at fwhm. Quantitative elemental composition measurements were made by correction of integrated peak intensities using Scofield factors[14] modified to account for the kinetic energy dependence of the electron mean free path.

The samples analyzed by EXAFS were embedded under an inert atmosphere in a mixture (50 wt % each) of reagent grade octacosane and hexatricontane and then pressed into wafers of uniform 10-mm thickness inside aluminum cells. Following this, 25 μm Kapton Windows were affixed using high vacuum grade epoxy resin. The amount of material embedded in each cell was chosen so as to give a total X-ray absorption of about 1.5 at the W–L_{III} edge (10.207 keV).

X-ray absorption data were collected at the National Synchrotron Light Source (Brookhaven National Laboratory, Upton, NY) on beamline X-11A. The monochromator was equipped with a Si(111) crystal pair, which was detuned by 10%, in order to eliminate the passage of synchrotron radiation harmonics through the exit beam. The data were obtained in transmission mode, using a pair of GSK Scientific ionization detectors filled with a flowing nitrogen/argon mixture (post-sample detector) and flowing nitrogen (pre-sample detector), respectively, both at atmospheric pressure. All samples were cooled to about 100 K before spectra were taken. For all samples and references, the W–L_{III} edge was scanned beginning at 200 eV before and ending at about 1300 eV above the edge. The monochromator energy origin was calibrated using a sample of tungsten powder which was held in a thin layer free of pinholes.

Normalization of the X-ray absorption data to the edge height and extraction and k-weighting of the EXAFS $\chi(k)$ function were performed according to standard methods.[15,16] Before transforming the X-ray absorption data to momentum space, the absorption threshold was calibrated by linear extrapolation of the pre-edge (−200 to −30 eV) and post-edge (50 to 200 eV) regions across the edge and then selecting the datapoint midway between these lines and setting its abcissa to zero energy. Next, a linear baseline was calculated by fitting the region from about 100 eV above the edge to the end of the dataset; this was subtracted from the data. Following this, the data were truncated to include the range containing the EXAFS information (15 to 1275 eV above the edge). After transforming into k-space (k^1 or k^3 weighted) and dividing by the absorption edge, a cubic spline fit was applied as further correction for low-frequency oscillations in the background. The data were next Fourier transformed over the range 2.76–16.20 $Å^{-1}$.

Isolation of the EXAFS due to photoelectron backscattering from the selected coordination shells was accomplished by the technique of Fourier filtering[15,16] and backtransforming into k-space. In all cases, a symmetric Hanning apodization function (with a rectangular section 70% of the total width) was used as the filtering window. The overall window width was chosen to be 1.1 Å in all cases involving k^1 weighted datasets and

(8) Ozin, G. A.; Malek, A.; Prokopowicz, R. A.; Macdonald, P. M.; Özkar, S.; Moller, K.; Bein, T. In New Directions in Zeolite Chemistry. *Mat. Res. Soc. Symp. Proc.* **1991**, *233*, 109.

(9) Dwyer, J.; Dyer, A. *Chem. Ind.* **1984**, 237 (and references cited therein).

(10) Özkar, S.; Ozin, G. A.; Moller, K.; Bein, T. *J. Am. Chem. Soc.* **1990**, *112*, 9595.

(11) Ozin, G. A.; Goodber, J. P. *J. Phys. Chem.* **1988**, *92*, 4980.

(12) Swift, P. *Surf. Interfac. Anal.* **1982**, *4*, 47. *ASTM Standard E 105* **1984**, *03.06*.

(13) Bryson, C. E. *Surf. Sci.* **1987**, *189/190*, 50.

(14) Scofield, J. H. *J. Electron Spectrosc.* **1976**, *8*, 129.

(15) Sayers, D. E.; Bunker, B. A. *X-ray Absorption: Principles, Applications, Techniques of EXAFS, SEXAFS and XANES. Chemical Analysis*; Koningsberger, D. C., and Prins, R., Eds.; Wiley & Sons; New York, 1988; Vol. 92.

(16) Lee, P. A.; Citrin, P. H.; Eisenberger, P.; Kincaid, B. M. *Rev. Mod. Phys.* **1981**, *53(4)*, 769.

Table I. Tungsten 4f Binding Energies (in eV, referenced to C(1s) at 284.9 eV)

sample	binding energy $W(4f_{7/2})$	$W(4f_{5/2})$	ref
bulk WO_3	35.5	37.6	30
bulk WO_2	32.5	34.6	31
$Na_2[W_2O_2(\mu\text{-}O)_2(\mu\text{-EDTA})]$	33.9	36.0	19
$Pt/WO_3\text{–}SiO_2$	36.6	38.7	32
$Pt/WO_{2.5}\text{–}SiO_2$	34.7	36.8	32
$Pt/WO_2\text{–}SiO_2$	33.6	35.7	32
$16WO_3\text{–}Na_{56}Y$	36.2	38.2	
$16WO_{2.5}\text{–}Na_{56}Y$	35.6	37.7	
$32WO_{2.5}\text{–}Na_{56}Y$	35.5	37.5	
$16WO_2\text{–}Na_{56}Y$	34.1	36.1	

W–O backscattering shells, and 0.9 Å in all cases involving k^3 weighted data and W–W shells.

Determination of the structural parameters (interatomic distances, coordination numbers, static disorder and inner potential) of the samples was made by simultaneous least-squares fitting of each filtered, back-transformed dataset using phase and amplitude functions extracted from the reference compounds, and an equation[16] which is applicable to the standard analysis of L_{III}-edge EXAFS. For the coordination shells containing oxygen backscatterers, the W–O shell in Na_2WO_4 was used to provide the reference amplitude and phase shift functions; for the coordination shells containing tungsten backscatterers, the phase and amplitude functions were extracted from the Re–L_{III} EXAFS of a sample of ReO_2. The latter compound was chosen instead of WO_3 since its structure has a well-defined unique Re–Re distance, whereas in WO_3 there is a distribution of W–W distances. The principles of phase and amplitude transferability between Re–Re and W–W scattering are taken to be valid[16] due to the similarity in their atomic numbers.

Results and Discussion

Using sequential saturation filling, photooxidation procedures identical with those described previously,[5] samples of $n[W(CO)_6]\text{–}Na_{56}Y$ were synthesized and then transformed to the respective tungsten(VI) oxide products $n[WO_3]\text{–}Na_{56}Y$ encompassing the entire composition range $0 < n \leq 32$. Each of these samples was then converted, by means of a temperature-programmed vacuum thermally-induced reductive-elimination of O_2 at 300 and 400 °C, into the corresponding $n[WO_{2.5}]\text{–}Na_{56}Y$ and $n[WO_2]\text{–}Na_{56}Y$ materials. These were then subjected to a multiprong analysis involving a combination of informative spectroscopy, diffraction, and microscopy probes together with elemental analysis, the goal being to elucidate key structural, bonding, and electronic properties of the imbibed tungsten oxide guests in $n[WO_{3-x}]\text{–}Na_{56}Y$ over the compositional field $0 < n \leq 32$ and $0 \leq x \leq 1$.

(A) Stoichiometries and Oxidation States. Thermal treatment of $n[WO_3]\text{–}Na_{56}Y$ shows that the evolution of O_2 begins around 200 °C to yield royal blue ($0 < n \leq 8$) or metallic blue-grey ($8 \leq n \leq 32$) materials with W:O = 1:2.5 at 300 °C. Further evolution of O_2 occurs between 300 and 400 °C to eventually yield essentially white ($0 < n \leq 8$) or greyish off-white ($8 \leq n \leq 32$) materials having W:O = 1:2. Quantitative reversal of this process can be achieved at 300 °C in O_2, recreating the original material $n[WO_3]\text{–}Na_{56}Y$ but apparently bypassing the intermediate phase $n[WO_{2.5}]\text{–}Na_{56}Y$. These observations provide compelling evidence for the reductive-elimination oxidative-addition sequence of reactions:

$$n[WO_3]\text{–}Na_{56}Y \xrightarrow[\text{vacuum}]{300\ ^\circ C} n[WO_{2.5}]\text{–}Na_{56}Y \xrightarrow[\text{vacuum}]{400\ ^\circ C} n[WO_2]\text{–}Na_{56}Y$$

$$n[WO_3]\text{–}Na_{56}Y \xleftarrow{300\ ^\circ C,\ O_2} n[WO_2]\text{–}Na_{56}Y$$

The XPS $W(4f_{7/2})$ = 36.2 eV core level binding energies (Figure 1, Table I) of $16[WO_3]\text{–}Na_{56}Y$ is clearly characteristic of W^{6+} with an upward energy shift of roughly 5.9 eV compared to the W^0 precursor $16[W(CO)_6]\text{–}Na_{56}Y$ and consistent with the W:O = 1:3 stoichiometry for the WO_3 guest. On passing to $16[WO_2]\text{–}Na_{56}Y$, the corresponding $W(4f_{7/2})$ = 34.1 eV core level ionization energy is diagnostic of W^{4+} (Table I), in line with the

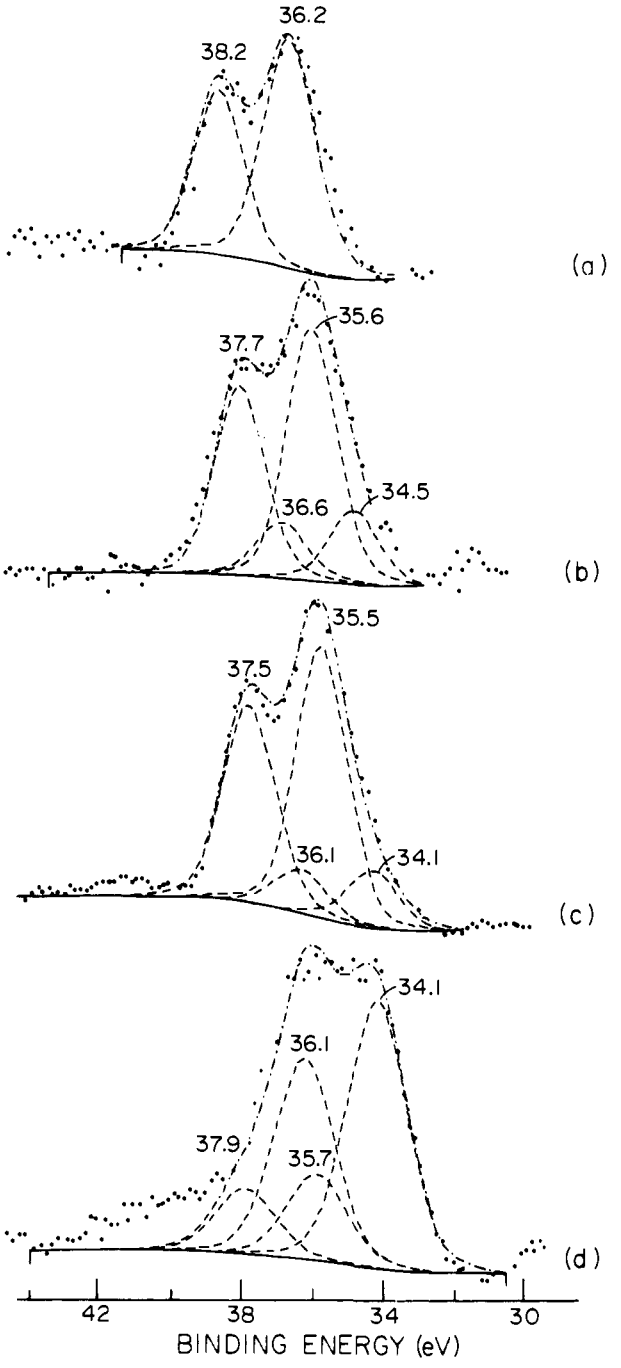

Figure 1. W(4f) XPS spectra of $n[WO_{3-x}]\text{–}Na_{56}Y$: (a) $n = 16$, $x = 0$; (b) $n = 16$, $x = 0.5$; (c) $n = 32$, $x = 0.5$; (d) $n = 16$, $x = 1$. Note that samples (b) and (c) intentionally contained about 20% of (d), and (d) contained about 20% of (b), to assist with the assignment of oxidation states in the aforementioned samples.

W:O = 1:2 stoichiometry for the WO_2 guest. The intermediate oxide $16[WO_{2.5}]\text{–}Na_{56}Y$ displays its corresponding core level ionization energy of $W(4f_{7/2})$ = 35.6 eV, which is intermediate between those of $16[WO_3]\text{–}Na_{56}Y$ and $16[WO_2]\text{–}Na_{56}Y$, signalling the existence of a W^{5+} rather than a mixed valence W^{4+}/W^{6+} species (Table I) consistent with the W:O = 1:2.5 stoichiometry for the $WO_{2.5}$ guest. Note that all of the $n[WO_{3-x}]\text{–}Na_{56}Y$ samples are EPR silent (300–120 K) but all yield high-quality ^{23}Na MAS-DOR-NMR spectra (see later). This implies that the entire series is diamagnetic with spin-paired electronic ground states for the W^{4+}-, W^{5+}-, and W^{6+}-containing materials.

All analytical techniques applied to this system demonstrate that each of the impregnation, photooxidation, and thermal treatment steps is clean and quantitative. Every sample exhibits

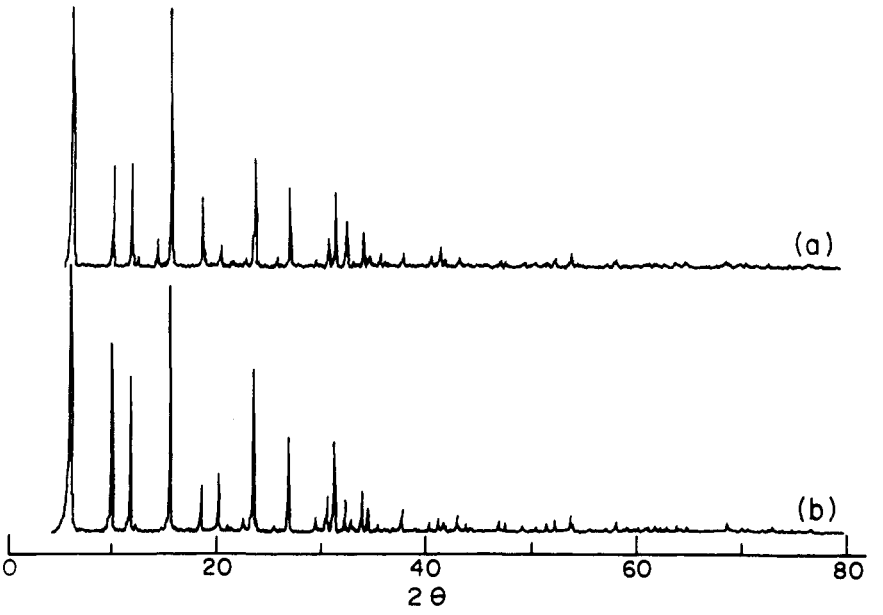

Figure 2. High-resolution powder X-ray diffraction data for (a) dehydrated $Na_{56}Y$ and (b) $16[WO_3]$–$Na_{56}Y$.

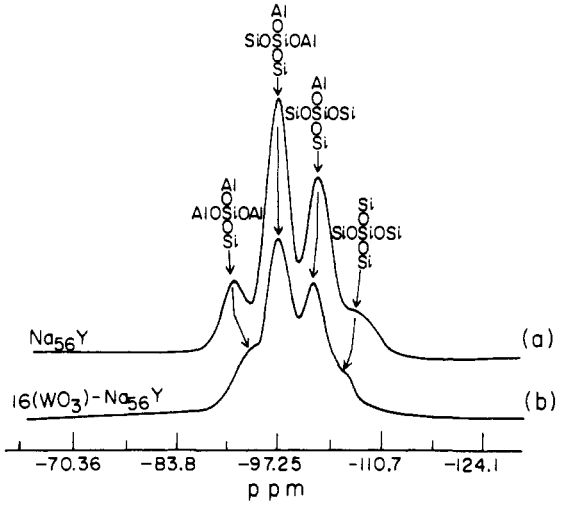

Figure 3. ^{29}Si MAS-NMR spectra of (a) dehydrated $Na_{56}Y$ and (b) $16[WO_3]$–$Na_{56}Y$.

a homogeneous appearance. In brief, quantitative PXRD, STEM-EDX, $^{29}Si/^{27}Al$ MAS-NMR, and XPS methods inform one that throughout the above procedures the following apply: (a) the crystal morphology of the $Na_{56}Y$ host remains unaltered; (b) the degree of crystallinity of the host is maintained (Figure 2); (c) the integrity of the framework stays intact (Figure 3); (d) the unit cell dimension of the cubic $Na_{56}Y$ host is essentially unaltered at a_0 = 24.690–24.694 Å for n = 0–32 (Figure 2); (e) there exists no evidence for the formation of bulk WO_{3-x} oxides (Figure 2); (f) the surface W:Na:Al elemental ratios are always close to, but slightly less than, the bulk elemental analysis; (g) no superlattice reflections are observed (Figure 2); and (h) there is no sign of carbon deposition at the 1000-ppm detection level (Figure 4).

Taken together, the above observations point to a sequence of events in which all WO_{3-x} moieties remain internally confined and homogeneously dispersed throughout the internal void structure of the zeolite Y host. Additional support for the above proposals stems from high-resolution electron microscopy. A representative lattice image is shown for $12[WO_3]$–$Na_{56}Y$ recorded on a Hitachi H-600 at 100 keV in Figure 5. Even though the specimen orientation, sample thickness, and depth of focus are not quantitatively defined in this experiment, it is nevertheless clear from this micrograph that the WO_3 guests (W_2O_6 dimers in 6 out of 8 α-cages—see later) are apparently internally confined, randomly

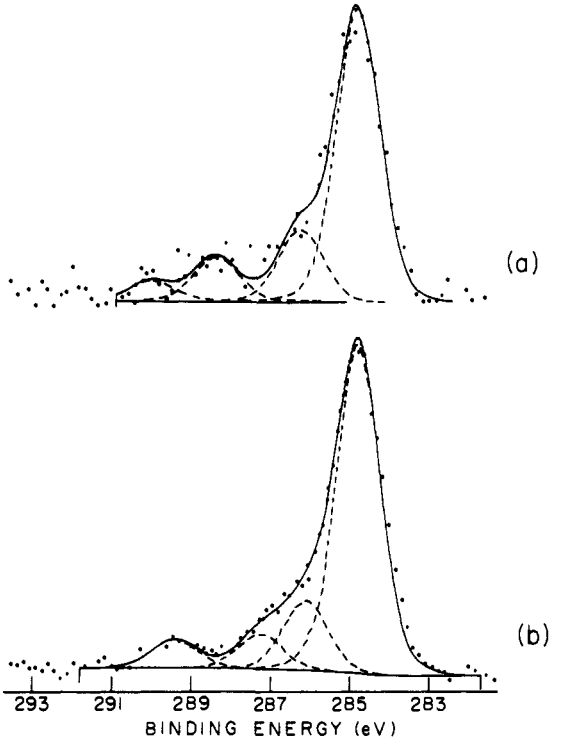

Figure 4. C(1s) XPS spectra of (a) dehydrated $Na_{56}Y$ and (b) $16[WO_3]$–$Na_{56}Y$.

organized, and not segregated into domains. Also, in agreement with the conclusions drawn from the XPS analysis, one observes a slight depletion of WO_3 guests in the first 30 Å or so of the external surface regions of the $Na_{56}Y$ host crystal, Figure 5.

Adsorption-induced ^{23}Na DOR-NMR chemical shifts (Figure 6), FAR-IR Na^+ translatory mode frequency shifts, and MID-IR $\nu(OH_\alpha)$ hydrogen-bonding shifts[6] provide direct and complimentary evidence for the anchoring of WO_{3-x} moieties to α-cage Na^+ cations in $n[WO_{3-x}]$–$Na_{56-m}H_mY$ (where m = 8, 16), see later. These experiments provide additional support for the homogeneity of the distribution of entrapped WO_{3-x} guests and moreover enable one to monitor the birth and population growth of these moieties over the entire composition field. In particular, it appears that at the special values of half-loading (n = 16) and full-loading (n = 32) one has created ordered supralattices containing $2(WO_{3-x})$ and $4(WO_{3-x})$ guests per α-cage, respectively.

Figure 5. High-resolution transmission electron micrograph lattice image of $12[WO_3]$–$Na_{56}Y$.

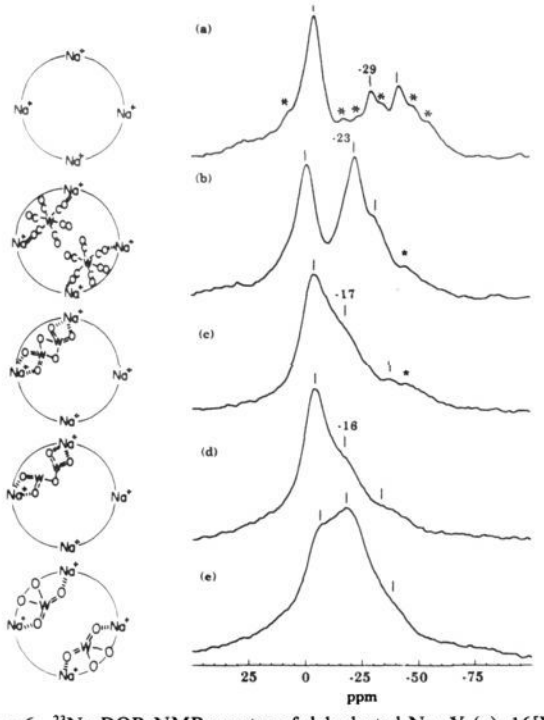

Figure 6. ^{23}Na DOR-NMR spectra of dehydrated $Na_{56}Y$ (a), $16[W(CO)_6]$–$Na_{56}Y$ (b), and oxidation products $16[WO_3]$–$Na_{56}Y$ (c), $16[WO_{2.5}]$–$Na_{56}Y$ (d), and $16[WO_2]$–$Na_{56}Y$ (e). The asterisks indicate spinning side bands.

It seems that over the entire compositional field of $n[WO_{3-x}]$–$Na_{56}Y$, the WO_{3-x} guests exhibit a rather special chemical affinity for, and spatial compatibility with, the internal void environment of the $Na_{56}Y$ host.

(B) Structural Data Derived from EXAFS Analysis. EXAFS W L_{III}-edge structure analysis has been successfully applied to the photooxidation products $n[WO_3]$–$Na_{56}Y$ (n = 16, 28, 32) and thermal reductive-elimination products $n[WO_{2.5}]$–$Na_{56}Y$ (n = 16, 32) and $n[WO_2]$–$Na_{56}Y$ (n = 16, 32). A summary of crystallographic data of key reference compounds is presented in the footnote of Table II. Representative examples of k^1 and k^3-weighed Fourier transform magnitudes as well as the inverse Fourier transforms of selected filtered shells and their least-squares fits are shown in Figures 7–9. Table II lists the derived structural data for all of the samples analyzed by EXAFS in this study and those of the previous study.[7]

Table II. The Structural Parameters Determined by Analysis of the W L_{III}-Edge EXAFS Data for $n[WO_{3-x}]$–$Na_{56}Y$ Samples, Where $0 < n \leq 32$ and $0 \leq x \leq 1$[a]

sample	atom pair	coord no.	bond distance, Å	static disorder, Å^2	inner potential, eV
$16[WO_3]$–$Na_{56}Y$	W–O	2.2	1.77	0.0008	3.8
	W–O	1.8	1.94	−0.0009	3.8
	W–W	1.3	3.30	0.0019	−6.9
$28[WO_3]$–$Na_{56}Y$	W–O	2.2	1.75	0.0030	3.6
	W–O	2.2	1.95	0.0010	−3.9
	W–W	1.4	3.24	0.0047	−3.5
$32[WO_3]$–$Na_{56}Y$	W–O	1.7	1.78	−0.0004	4.1
	W–O	1.9	1.96	0.0008	2.4
	W–W	1.4	3.31	0.0009	−10.0
$16[WO_{2.5}]$–$Na_{56}Y$	W–O	2.1	1.77	0.0009	6.1
	W–O	1.1	1.94	−0.0011	2.8
	W–W	1.3	3.30	0.0028	−10.0
$32[WO_{2.5}]$–$Na_{56}Y$	W–O	2.2	1.83	0.0048	5.0
	W–O	0.8	2.00	−0.0034	−4.3
	W–W	3.0	3.30	0.0036	−5.5
$16[WO_2]$–$Na_{56}Y$	W–O	4.1	1.81	0.0028	0.4
$28[WO_2]$–$Na_{56}Y$	W–O	4.1	1.79	0.0024	0.8
$32[WO_2]$–$Na_{56}Y$	W–O	4.0	1.84	0.0040	1.9

[a] The compounds Na_2WO_4 and ReO_2 were used as phase and amplitude references in the above analyses. Crystallographic data[18] indicate a coordination number of 4 and a bond length of 1.819 Å for W–O and N = 1 and r = 2.610 Å for Re–Re.

(i) Photooxidation Product: $n[WO_3]$–$Na_{56}Y$, n = 16, 28, 32. The Fourier transform magnitude of the (normalized, background isolated) EXAFS data for the sample $32[WO_3]$–$Na_{56}Y$ is shown in Figure 7, along with the Fourier filtering windows used in the inverse transformation procedures for both the W–O and W–W shells; the inverse transformed data and least-squares fits are also depicted in the figure. A qualitative comparison of the k^1-weighed Fourier transforms of all three samples $n[WO_3]$–$Na_{56}Y$ for n = 16, 28, 32 shows them to be remarkably similar, immediately implying that the encapsulated W_2O_6 dimers established previously[7] by EXAFS to be present in the n = 16, 28 samples also exist in the fully loaded sample n = 32. By using a similar fitting procedure for the n = 32 sample (Figure 7) as used earlier[7] for n = 16, 28, one discovers that the quantitative details of the structure analysis for all three samples (Table II) are indeed very similar. As before, results indicate two short terminal W–O bonds (R_{wo} = 1.75–1.78 Å, N_o = 1.7–2.2) and two long bridging W–O bonds (R_{wo} = 1.94–1.96 Å, N_o = 1.8–2.2). Application of the curve-fitting procedure to the k^3-weighted datasets yielded, again with similarity among all three samples, a short distance to a second tungsten (R_{ww} = 3.24–3.31 Å, N_w = 1.3–1.4). This bond length and coordination number information for n = 16, 28, 32 samples is best interpreted in terms of the formation of a *single kind* of tungsten(VI) oxide dimer moiety namely W_2O_6, having one per α-cage for n = 16, two per α-cage for n = 32, and some combination of these two extremes (half and full filling) for the intermediate loading n = 28. The terminal dioxotungsten bond lengths of 1.75–1.78 Å found in these dimers fall within a range between those normally observed[17,18] for compounds having tungsten–oxygen formal bond orders of 2 (e.g., 1.69–1.70 Å in $W_6O_{19}^{2-}$) and 1.5 (e.g., 1.82 Å in WO_4^{2-}). This indirectly implies the existence of anchoring interactions between the terminal

(17) Day, V. W.; Klemperer, W. G. *Science* **1985**, *228*, 533.
(18) Okada, K.; Morikawa, H.; Marumo, F.; Iwai, S. *Acta Crystallogr.* **1974**, *B30*, 1872. Magnêli, A. *Acta Crstallogr.* **1956**, *9*, 1038.

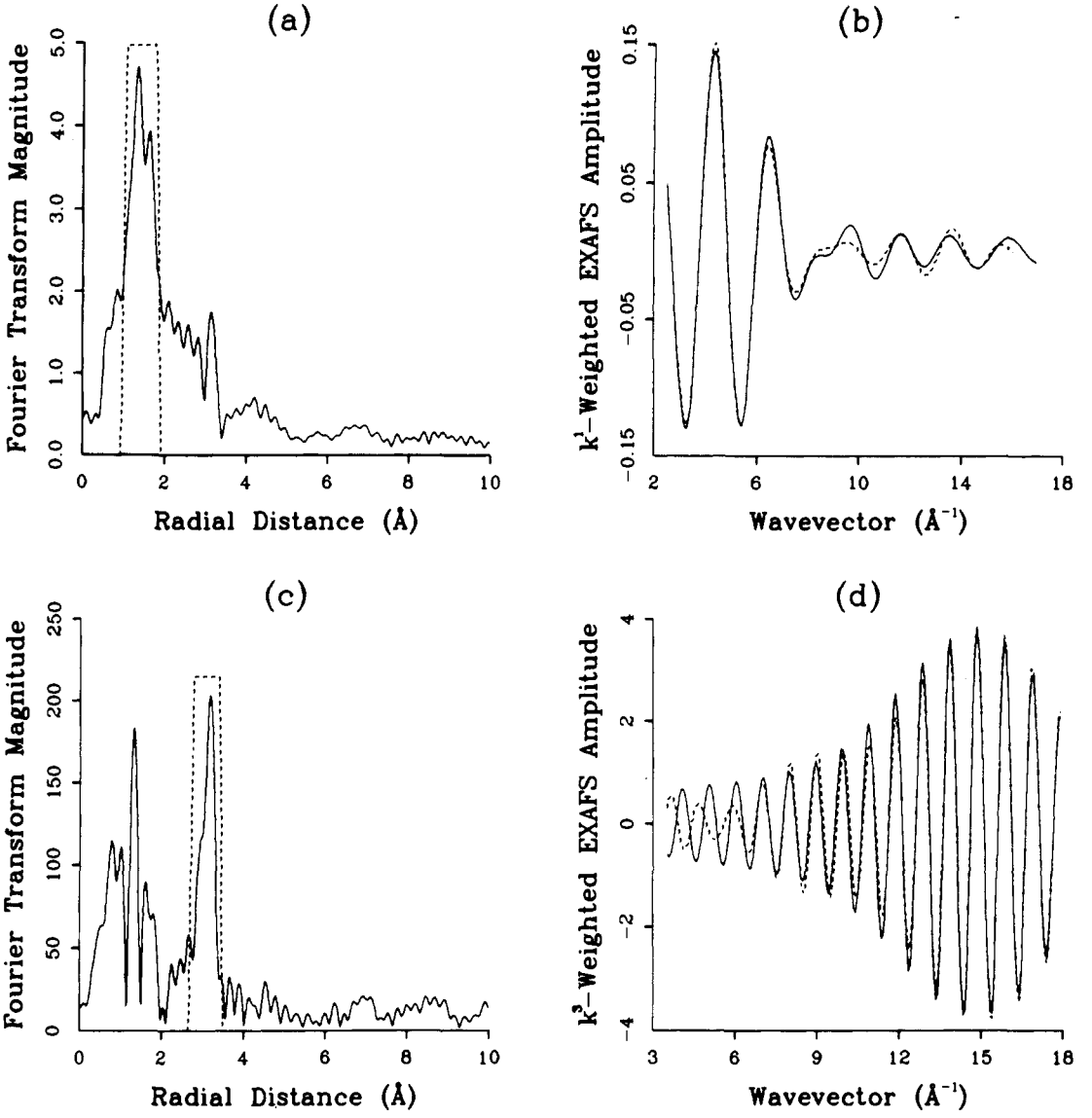

Figure 7. EXAFS results for $32[WO_3]$–$Na_{56}Y$: (a) k^1-weighted Fourier transform magnitude showing the filtering window used to isolate the W–O shells; (b) inverse Fourier transform of (a) and least-squares fit of the data; (c) k^3-weighted Fourier transform magnitude showing the filtering window used to isolate the W–W shells; and (d) inverse Fourier transform of (c) and least-squares fit of the data.

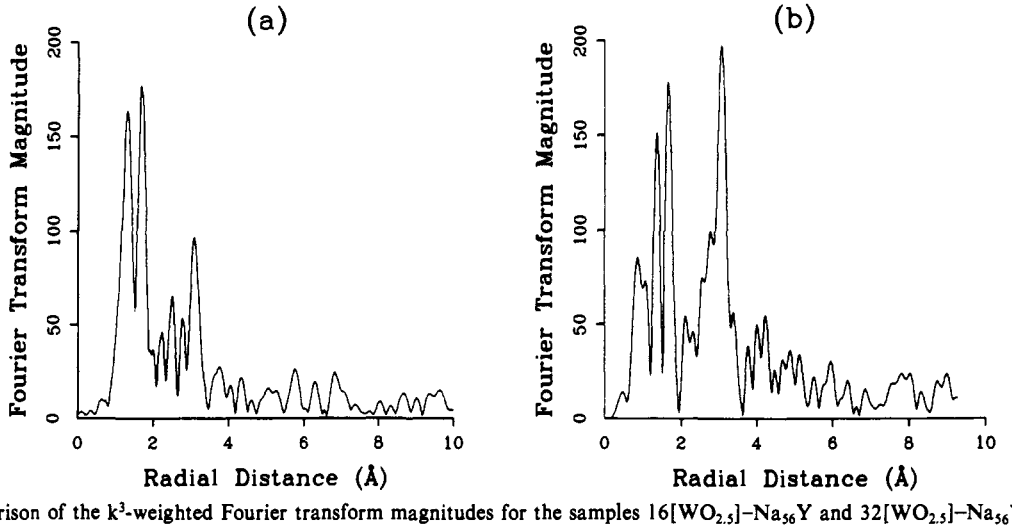

Figure 8. Comparison of the k^3-weighted Fourier transform magnitudes for the samples $16[WO_{2.5}]$–$Na_{56}Y$ and $32[WO_{2.5}]$–$Na_{56}Y$.

dioxotungsten groups of the W_2O_6 guest and extraframework α-cage Na^+ cations of the $Na_{56}Y$ host, which is in agreement with the conclusion drawn from chemical and spectroscopic measurements, described in the other sections of this work. The tungsten–oxygen bond length of 1.94–1.96 Å found for the bridging $W(\mu\text{-}O)_2W$ unit of the dimer falls within the range expected for doubly oxygen bridged W^{6+} species, e.g., 1.92 Å found[17] in $W_6O_{19}^{2-}$. The dimer structural unit

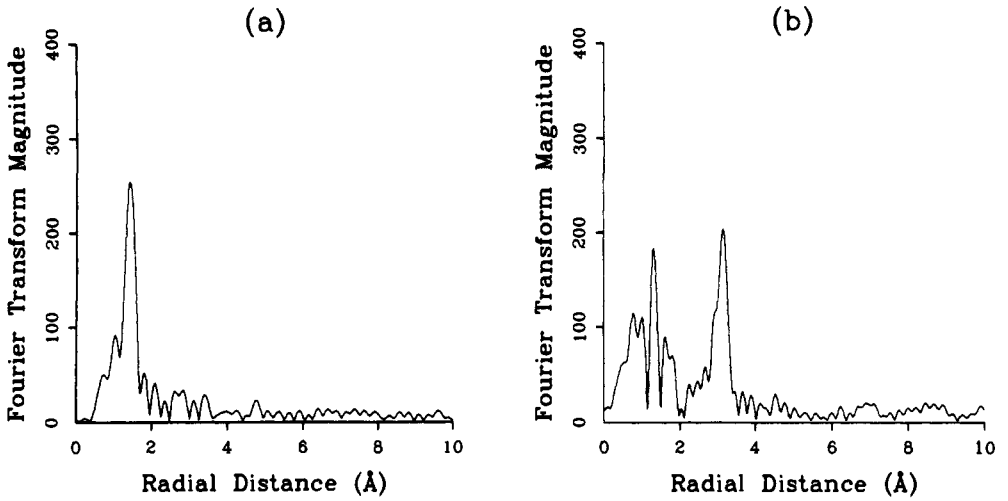

Figure 9. k^3-weighted Fourier transform magnitude showing (a) lack of evidence of W–W pairs in $32[WO_2]$–$Na_{56}Y$ and (b) a W–W contribution in $32[WO_3]$–$Na_{56}Y$.

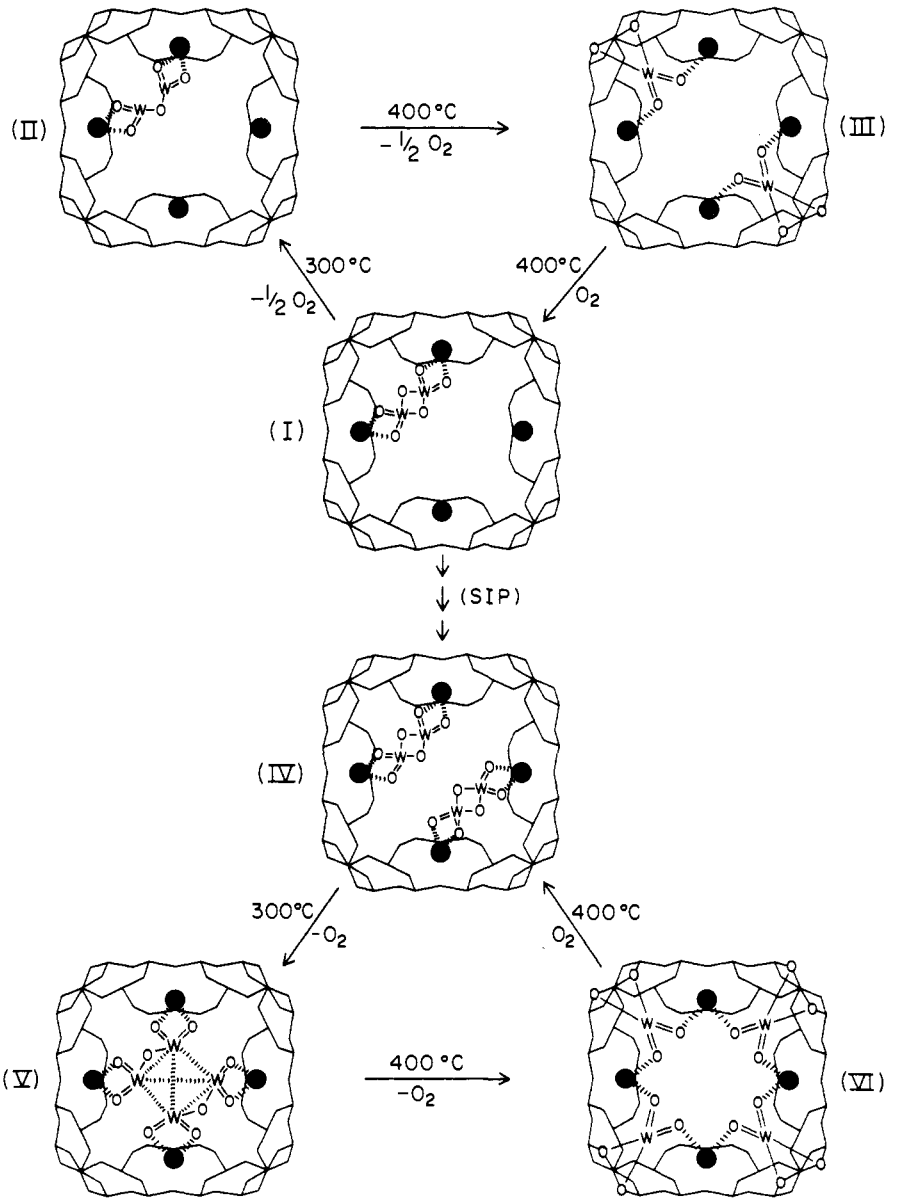

Figure 10. Illustration of structure and anchoring of α-cage encapsulated molecular tungsten oxide species in half-loaded and fully-loaded samples $16[WO_{3-x}]$–$Na_{56}Y$ and $32[WO_{3-x}]$–$Na_{56}Y$, where $x = 0, 0.5, 1$. Note that SIP denotes a sequential impregnation photooxidation process; see text for details.

$(ZONa)...O_2W^{6+}(\mu\text{-}O)_2W^{6+}O_2...(NaOZ)$ illustrated in Figure 10 is fully consistent with the structural data derived from analysis of the EXAFS data for samples covering the composition range n = 16, 28, 32. The sequential addition of WO_3 units to the $16[WO_3]$–$Na_{56}Y$ tungsten(VI) oxide supralattice composed of α-cage encapsulated W_2O_6 dimers, eventually to form fully filled $32[WO_3]$–$Na_{56}Y$, is visualized as a continued increase in the W_2O_6 dimer population, causing an accumulation of α-cage dimers-of-dimers W_2O_6 rather than cluster accretion to α-cage trimers W_3O_9 and/or tetramers W_4O_{12}, Figure 10. Examples of complexes which actually contain "pieces" of the dimeric W_2O_6 species found in $n[WO_3]$–$Na_{56}Y$ can be found in the literature.[1,19,20]

(ii) First-Stage Thermal Vacuum Reductive-Elimination Product: $n[WO_{2.5}]$–$Na_{56}Y$, n = 16, 28, 32. Analysis of the EXAFS data for the samples $n[WO_{2.5}]$–$Na_{56}Y$ (n = 16, 32) produced by reductive-elimination of O_2 from $n[WO_3]$–$Na_{56}Y$ at 300 °C yielded results which are presented in Figure 8. A qualitative comparison of the k^1- and k^3-weighted Fourier transform magnitudes of the $16[WO_{2.5}]$–$Na_{56}Y$ and $32[WO_{2.5}]$–$Na_{56}Y$ samples among themselves and with those of the corresponding $n[WO_3]$–$Na_{56}Y$ samples shows them to be strikingly similar in terms of peak amplitudes. Here it can be determined that the $16[WO_{2.5}]$–$Na_{56}Y$ sample displays two short terminal W–O bonds (R_{wo} = 1.77 Å, N_o = 2.1) but only one long bridging W–O bond (R_{wo} = 1.94 Å, N_o = 1.1) together with a short distance to a second tungsten (R_{ww} = 3.30 Å, N_w = 1.3). This bond length and coordination number information for $16[WO_{2.5}]$–$Na_{56}Y$ in conjunction with the XPS data presented earlier are consistent with the presence of a *single kind* of tungsten(V) oxide dimer moiety W_2O_5. The tungsten–oxygen terminal and bridge bond lengths are as expected for a $(ZONa)...O_2W^{5+}(\mu\text{-}O)W^{5+}O_2...(NaOZ)$ structural unit (Figure 10, two W^{5+} centers, with a single bent $W(\mu\text{-}O)W$ bridge bond and two terminal W=O bonds, the latter anchored to α-cage Na^+ cations) both essentially the same as the respective bonds found in the $(ZONa)...O_2W^{6+}(\mu\text{-}O)_2W^{6+}O_2...(NaOZ)$ moiety. The EPR silence and NMR activity (see later) for the W_2O_5 dimer present in every α-cage of $16[WO_{2.5}]$–$Na_{56}Y$ favors the existence of a diamagnetic spin-paired singlet electronic ground state for the $W^{5+}(\mu\text{-}O)W^{5+}$ d^1–d^1 centers, possibly superexchange coupled through the single μ-oxo bridge bond.

Comparison of the structural details of $16[WO_{2.5}]$–$Na_{56}Y$ and $32[WO_{2.5}]$–$Na_{56}Y$ shows that they are remarkably similar with respect to the tungsten–oxygen bond distances and coordination numbers and with respect to the tungsten–tungsten distances (R_{ww} = 3.30 Å). However, the latter displays three neighboring tungstens (N_w = 3.0), whereas the number in the former case was about one (N_w = 1.3). An effect of this type was anticipated from qualitative inspection of differences in the W–W shell region in the k^3-weighted Fourier transform magnitudes for the n-$[WO_{2.5}]$–$Na_{56}Y$, n = 16, 32 samples (Figure 8). The bond length and coordination number information for $32[WO_{2.5}]$–$Na_{56}Y$, together with the XPS data presented earlier and ^{23}Na MAS-DOR-NMR data presented later, are consistent with the presence of a *single kind* of tungsten(V) oxide tetramer moiety W_4O_{10} (anchored through the oxygen end of its terminal oxotungsten bonds to α-cage Na^+ cations), which is best formulated as $(ZONa)_2...O_4W_2^{5+}(\mu\text{-}O)_2W_2^{5+}O_4...(NaOZ)_2$, Figure 10.

Because of the observed EPR silence and NMR activity (see later) for the tetramer present in every α-cage of $32[WO_{2.5}]$–$Na_{56}Y$, this tetramer is formulated as containing two diamagnetic spin-paired singlet electronic ground state $(ZONa)...O_2W^{5+}(\mu\text{-}O)W^{5+}O_2...(NaOZ)$ d^1–d^1 dimer units. These are "intramolecularly" coupled (possibly superexchange) across their individual μ-oxo bridge bond and "intermolecularly" coupled (possibly exchange) across the d^1–d^1 dimer units. This concept

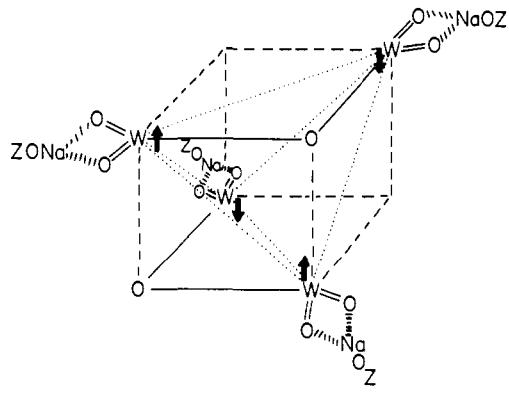

Figure 11. Representation of the structure of the sodium cation anchored diamagnetic exchange-coupled W_4O_{10} tetramer found in the α-cage of $32[WO_{2.5}]$–$Na_{56}Y$. The bold arrows indicate the unpaired electron spins on the individual W^{5+} centers.

is illustrated in Figure 11. Much more work will be required to throw any further light on this unique tetramer. This would involve, in particular, details of the intra- and intercluster electronic interactions as well as the possibility of "face-edge-face" exchange dynamics of the μ-oxo bridge oxygen atom, with respect to the essentially tetrahedral array of coupled W^{5+} centers.

(iii) Second-Stage Thermal Vacuum Reductive-Elimination Product: $n[WO_2]$–$Na_{56}Y$, n = 16, 28, 32. The same analysis procedure for the W-L_{III} EXAFS data as that described for $n[WO_3]$–$Na_{56}Y$ and $n[WO_{2.5}]$–$Na_{56}Y$ was applied to the 400 °C reduction products $n[WO_2]$–$Na_{56}Y$. The results for the sample $32[WO_2]$–$Na_{56}Y$ are presented in Figure 9 and included along with results from the earlier analyses[7] in Table II. A qualitative comparison of the k^1- and k^3-weighed Fourier transform magnitudes of the $n[WO_2]$–$Na_{56}Y$ samples n = 16, 28, 32 among themselves and with the aforementioned materials $n[WO_{3-x}]$–$Na_{56}Y$ (x = 0 and 0.5) demonstrates that there is remarkable similarity among the samples having x = 1 and n = 16, 28, 32 but that these samples are markedly different from those having other values of x (Figures 7–9). In particular the EXAFS data for the $n[WO_2]$–$Na_{56}Y$ series indicate a first shell containing only one W–O distance and no evidence of any W–W scattering contribution. Quantitative details are listed in Table II. Inspection of the tungsten–oxygen bond lengths and coordination numbers shows that the $n[WO_2]$–$Na_{56}Y$ samples contain a four-coordinate tungsten oxide moiety having R_{wo} = 1.79–1.84 Å, N_o = 4.0–4.1, which are very similar to the corresponding values for the Na_2WO_4 reference compound given in the footnote of Table II. That there is no evidence of W–W backscatter pairs implies that the distances between the tungsten centers in WO_2 must be much greater than in the aforementioned W_2O_6, W_2O_5 dimer, and W_4O_{10} tetramer species.

This information, the XPS data presented earlier, and the ^{23}Na MAS-DOR-NMR data presented below are consistent with the presence of a *single kind* of tungsten(IV) oxide WO_2 monomer, which is primarily anchored via the tungsten center to two oxygens possibly of a framework 4-ring coordination site, with secondary interactions through the oxotungsten bonds to α-cage site II Na^+ cations, namely $(ZO)_2...W^{4+}O_2...(NaOZ)_2$ (Figure 10). The observed EPR silence and NMR activity (see below) for these species is best reconciled in terms of diamagnetic low-spin monomeric W^{4+} centers, which is not unreasonable for a third-row transition element complex.[1]

A summary of the structures and anchoring schemes proposed for α-cage encapsulated "molecular" tungsten oxides in n-$[WO_{3-x}]$–$Na_{56}Y$ for half and full-loading samples n = 16, 32 and x = 0, 0.5, 1 is illustrated in Figure 10.

(C) ^{23}Na MAS-DOR-NMR Probes: Exploring Anchoring Sites. We have recently shown[6] that adsorption-induced ^{23}Na MAS-NMR chemical shifts and intensity changes provide direct evidence for the anchoring of W_2O_6 dimers to α-cage Na^+ cations in n-$[WO_3]$–$Na_{56}Y$ over the composition range $0 < n \leq 28$. In this section we apply the ^{23}Na MAS-NMR method to the entire series

(19) Ikari, S.; Sasaki, Y.; Ito, T. *Inorg. Chem.* **1989**, *28*, 447. Ikari, S.; Sasaki, Y.; Nagasawa, A.; Kabuto, C.; Ito, T. *Inorg. Chem.* **1989**, *28*, 1248.
(20) Rau, M. S.; Kretz, C. M.; Mercando, L. A.; Geoffroy, G. L. *J. Am. Chem. Soc.* **1991**, *113*, 7420.
(21) Fitch, A. N.; Jobic, H.; Renouprez, A. *J. Phys. Chem.* **1986**, *90*, 1311.
(22) Jelinek, R.; Özkar, S.; Ozin, G. A. *J. Am. Chem. Soc.* **1992**, *114*, 4907.

$n[WO_{3-x}]$–$Na_{56}Y$ over the full composition field $0 < n \leq 32$ and $0 \leq x \leq 1$ in a systematic attempt to explore further details of the anchoring sites in these interesting systems. Furthermore, we compare the results of ^{23}Na DOR-NMR with ^{23}Na MAS-NMR measurements for these samples, which serve to demonstrate the spectacular enhancement of resolution obtained by the former method relative to the latter for the quadrupolar ^{23}Na ($I = {}^3/_2$) nucleus.

DOR-NMR spectroscopy of solids containing quadrupolar nuclei annihilates second-order anisotropic line-shift and broadening contributions which are not averaged out in the corresponding MAS-NMR experiment.[23,24] Under these circumstances one is able to obtain high-resolution NMR spectra of, for example, the individual Na^+ sites in $Na_{56}Y$ (isotropic chemical and quadrupolar shifts, intensities, and relaxation times)[22] and how each of these is affected by the presence of an adsorbed guest.[25] Here the Na^+ chemical shifts are expected[6] to be sensitive to site-specific oxygen-framework and cation anchoring energetics. The corresponding intensities and line shapes should reflect the Na^+ site distribution, population, and dynamics.

Let us first focus attention on the ^{23}Na MAS-NMR spectrum of fully dehydrated $Na_{56}Y$ (XRD/ND site distribution:[21] I (7.1–7.7), I′ (13.4–18.6), II (29.4–32.0), III (6.5)). Here one observes a single broad asymmetric resonance center around −12 ppm. In striking contrast, the ^{23}Na DOR-NMR spectrum of this same material (Figure 6) vividly reveals that this signal in fact originates from a convolution of distinct Na^+ cation site resonances, which are assigned I (−5 ppm; double six-ring, hexagonal prism), II (−29 ppm; six-ring, α-cage), and I′ (−41 ppm; six-ring, β-cage).[22] All quoted chemical shifts in parentheses are referenced to solid NaCl.

The ^{23}Na DOR-NMR spectrum of virgin $Na_{56}Y$ at room temperature shown in Figure 6 has been assigned,[22] through a combination of site-selective Na^+ ion-exchange (e.g., $Na_{56-n}Tl_nY$) and site-selective Na^+ adsorption (e.g., $n[W(CO)_6]$–$Na_{56}Y$) thereby pinpointing I (−5 ppm), II (−29 ppm), and I′ (−41 ppm).

In $16[WO_{3-x}]$–$Na_{56}Y$, the ^{23}Na MAS-NMR spectra are only able to show that the W_2O_6 and W_2O_5 dimers and WO_2 monomers perturb one or more components of the high-field shoulder of the main resonance around −12 ppm, resulting in an increase in intensity between about −15 and −25 ppm. That this change is not the outcome of a second-order quadrupole line-shift or broadening effect can be seen from inspection of the corresponding ^{23}Na DOR-NMR spectra[25] (Figure 6). The W_2O_6 dimer, shown in Figure 10, is thought to possess a configuration in which the anchoring interaction involves the oxygen end of its two terminal oxotungsten bonds and two site II Na^+ cations. Accordingly, a significant decrease in the intensity of the ^{23}Na resonance ascribed to site II Na^+ cations is observed, relative to that corresponding to the $16[W(CO)_6]$–$Na_{56}Y$ precursor material. It is noteworthy that in the precursor material, as depicted in Figures 6b and 10, twice as many Na^+ cations were involved in anchoring. The signal due to the site II Na^+ in $16[WO_3]$–$Na_{56}Y$, Figure 6c, appears as a shoulder on the prominent downfield resonance and is located at around −17 ppm. This pronounced downfield shift from the original position of the site II signal in the precursor (at −23 ppm, Figure 6b) probably originates from the structural transformation experienced during conversion of the precursor $16[W(CO)_6]$–$Na_{56}Y$ to product $16[WO_3]$–$Na_{56}Y$. Such a transformation might significantly alter the environment and interaction strength of the anchoring site II Na^+ cations.

The first-stage thermal reduction product $16[WO_{2.5}]$–$Na_{56}Y$ consists of a supralattice of superexchange coupled (W^{5+}/W^{5+}) W_2O_5 dimers, whereas the final product $16[WO_2]$–$Na_{56}Y$ exists as separate WO_2 monomers, as illustrated in Figure 10. Inspection of the DOR-NMR spectra in Figure 6 supports this structural picture. Hardly any difference is observed between the ^{23}Na spectra of the W_2O_6 and W_2O_5 loaded samples (Figure 6, c and d, respectively). This is anticipated since the basic dimer structure and site II Na^+ anchoring interactions are maintained in both materials. On the other hand, the thermally reduced sample $16[WO_2]$–$Na_{56}Y$ contains WO_2 monomers, each of which interacts with two Na^+ anchoring cations, twice as many as the dimeric species. Indeed, the ^{23}Na DOR-NMR spectrum of this final product, shown in Figure 6e, features a prominent signal at around −17 ppm which is ascribed to the Na^+ anchoring cations at site II. This anchoring site II Na^+ resonance is broader than that corresponding to the parent material $16[W(CO)_6]$–$Na_{56}Y$, at −23 ppm (Figure 6b). This broadening might be brought about because of a relatively weak anchoring interaction between the oxygens in WO_2 and the site II Na^+ cations, which allows a larger distribution of Na^+ environments. The reader may refer to the discussion[22] of the site II Na^+ signal in dehydrated $Na_{56}Y$. Such interpretation is supported by spin–lattice relaxation measurements conducted in our laboratories, and might be related to a weaker Lewis basicity of the oxotungsten bond of WO_2, compared to that of the carbonyl group in the $W(CO)_6$ guest.[25]

As mentioned earlier, the ability to collect high-quality "normal" ^{23}Na MAS and DOR-NMR spectra for all of these systems supports the proposal that all of the WO_{3-x} moieties in the α-cage of the $Na_{56}Y$ are diamagnetic, with spin-paired electronic ground states. This point is further reinforced by the UV–visible spectroscopic studies of these species described in the next section.

On a final point, it is worth noting that the ^{29}Si MAS-NMR spectrum of $n[WO_3]$–$Na_{56}Y$ compared to that of $Na_{56}Y$ provides information on the kind of perturbation of the aluminosilicate framework which results from the anchoring of W_2O_6 dimers in the α-cages of $Na_{56}Y$, as well as conveying information on the maintenance of the lattice integrity mentioned earlier. Thus, it is interesting to note that the observed decrease in the separation between the high- and low-field $\delta Si(n Al)$ chemical shifts, namely $\Delta[\delta Si(0Al) - \delta Si(4Al)]$, on passing from $Na_{56}Y$ to $n[WO_3]$–$Na_{56}Y$ (Figure 3) parallels that which is observed on decreasing the Si/Al ratio from 2.75 to 1.19 in faujasite.[24] This implies charge transfer from the anchored W_2O_6 via the Na_{II}^+ cations to the framework of the $Na_{56}Y$, thereby increasing the oxygen framework charge density, which parallels the effect of making the host lattice more aluminous.

(D) Optical Reflectance Studies. Some valuable structure–electronic clues about the $n[WO_{3-x}]$–$Na_{56}Y$ materials can be obtained from their optical reflectance spectra. From inspection of some representative UV–visible spectral traces shown in Figure 12, one spots two informative effects. An intense broad blue visible band and a red-shifted UV band are observed on passing from $n[WO_3]$–$Na_{56}Y$ to $n[WO_{2.5}]$–$Na_{56}Y$. This blue band broadens and the UV band red shifts on passing from isolated ($n < 8$) to coupled ($8 \leq n \leq 32$) $n[WO_{2.5}]$–$Na_{56}Y$ materials. The blue band disappears and the UV band shifts even further red on passing from $n[WO_{2.5}]$–$Na_{56}Y$ to $n[WO_2]$–$Na_{56}Y$. The UV band red shifts again on passing from isolated ($n < 8$) to coupled ($8 \leq n \leq 32$) $n[WO_2]$–$Na_{56}Y$ materials, Figure 12.

Recall that the parents $n[WO_3]$–$Na_{56}Y$ display an $O^{2-}(2p\pi) \rightarrow W^{6+}(5d\pi)$ UV absorption which can be assigned to an interstate (HOMO-LUMO) LMCT excitation for the isolated W_2O_6 dimers ($n < 8$), as illustrated in the qualitative molecular orbital scheme shown in Figure 13. In the situation of electronically coupled W_2O_6 dimers ($8 \leq n \leq 32$), the loading-dependent red shifts of the UV absorption (Figure 12) suggest that it may be more appropriate to assign this absorption in terms of an interminiband[33] (MVB → MCB) transition, as illustrated in the qualitative electronic band energy level scheme shown in Figure 13.

The optical reflectance spectra in conjunction with the stoichiometry, structural, anchoring, electronic, and oxidation state clues for $n[WO_{3-x}]$–$Na_{56}Y$ described earlier permit one to assign the blue band in $n[WO_{2.5}]$–$Na_{56}Y$ ($n < 8$) as a $W^{5+} \rightarrow W^{5+}$ ligand-field (LF, noncentrosymmetric W_2O_5, spin and dipole

(23) Samoson, A.; Lippmaa, E.; Pines, A. *Mol. Phys.* **1988**, *65*, 1013. Chmelka, B. F.; Mueller, K. T.; Pines, A.; Stebbins, J.; Wu, Y.; Zwanziger, J. W. *Nature* **1989**, *339*, 42. Wrenwooten, E.; Mueller, K. T.; Pines, A. *Acc. Chem. Res.* **1992**, *25*, 209.

(24) Engelhard, G.; Michel, D. *High Resolution Solid State NMR of Silicates and Zeolites*; Wiley & Sons: New York, 1987.

(25) Jelinek, R.; Özkar, S.; Ozin, G. A.; Pastore, H. O. *J. Phys. Chem.* **1992**, *96*, 5949. Jelinek, R.; Özkar, S.; Ozin, G. A.; Pastore, H. O. *J. Am. Chem. Soc.* In press.

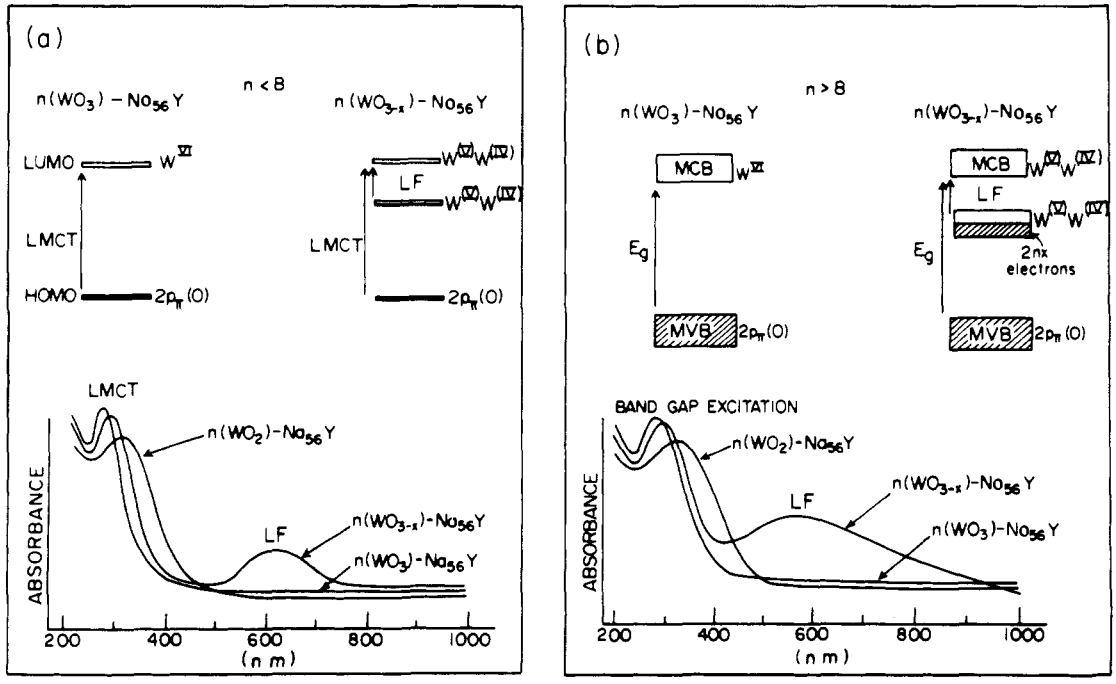

Figure 12. UV-visible reflectance spectra of $n[WO_{3-x}]$–$Na_{56}Y$ for (a) $n < 8$ and (b) $n > 8$, where $x = 0$, 0.5, 1.0.

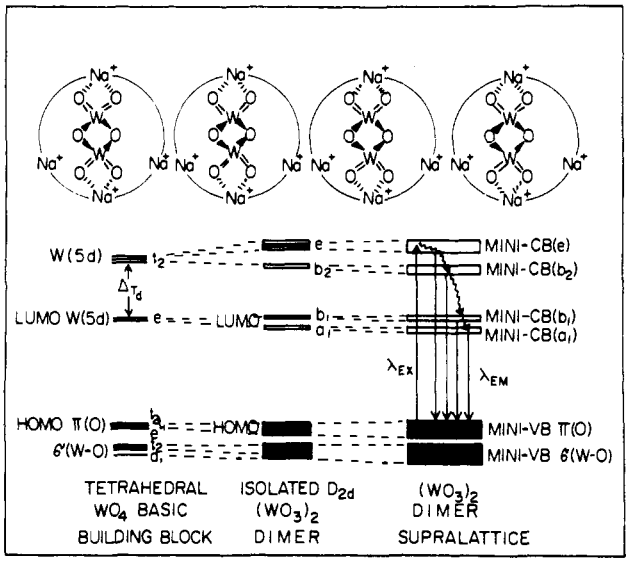

Figure 13. Qualitative miniband electronic scheme for $16[WO_3]$–$Na_{56}Y$.

allowed) transition, rather than the less likely $W^{4+} \rightarrow W^{6+}$ intervalence-charge transfer (IVCT) type, Figure 12. The UV band is then assigned to a $O^{2-}(2p\pi) \rightarrow W^{5+}(5d\pi)$ LMCT transition, Figure 12. Where the W_2O_5 moieties in $n[WO_{2.5}]$–$Na_{56}Y$ first begin to couple (through space or through zeolite framework) these LF and LMCT bands appear to broaden and/or red shift, Figure 12. The visible LF band disappears in $n[WO_2]$–$Na_{56}Y$ ($n \leq 8$) with concomitant red shifting of the $O^{2-}(2p\pi) \rightarrow W^{4+}(5d\pi)$ LMCT band. Similar shifting and broadening effects occur in $n[WO_2]$–$Na_{56}Y$ at $8 \leq n \leq 32$. In the case of the spin-paired Na^+ anchored W_2O_5 dimer moiety, it is not unreasonable to expect a $W^{5+} \rightarrow W^{5+}$ LF excitation in the visible region, whereas in the case of a low-spin oxygen framework tethered WO_2 monomer, the corresponding $W^{4+} \rightarrow W^{4+}$ LF excitation most likely shifts into the UV region, where it could be overlapped with and/or hidden by[26] the intense UV-LMCT band (Figure 12).

(E) Some Thoughts Concerning Possible Reaction Pathways for the Photooxidation of $n[W(CO)_6]$–$Na_{56}Y$ and Thermal Redox Reactions of $n[WO_{3-x}]$–$Na_{56}Y$. Photooxidation of $W(CO)_6$ in Ar/O_2 mixtures at 10 K has been shown to proceed through reaction intermediates *trans*-$WO_2(CO)_4$ and *cis*-$WO_2(CO)_2$ to yield monomeric bent (C_{2v}) WO_2, with the ligated carbonyls ending up as CO/CO_2 in a 1/5 ratio.[27] The monomer intermediate WO_2 is subsequently transformed[27] to monomeric triangular planar (D_{3h}) WO_3 via *cis*-$WO_2(O_2)$, in an oxygen atom transfer step between WO_2 and *cis*-$WO_2(O_2)$. Thermal oxidation of *fac*-$LW(CO)_3$ in H_2O_2/THF mixtures at 45 °C (where L = 1,4,7-triazocyclononane or *N,N',N''*-trimethyl-1,4,7-triazocyclononane) yields monomeric *fac*-LWO_3 complexes.[28] The lability of ligand stabilized trigonal pyramidal (C_{3v}) trioxotungsten(VI) units in these types of complexes is purportedly higher than that of the corresponding trioxomolybdenum(VI) ones. Significantly the photooxidation products of $n[M(CO)_6]$–$Na_{56}Y$ (M = Mo, W) are, respectively, anchored W_2O_6 dimers $(ZONa)...O_2W^{6+}(\mu\text{-}O)_2W^{6+}O_2...(NaOZ)$ and MoO_3 monomers $(ZO)_2...MoO_3...(NaOZ)_2$, the difference possibly originating in the kinetic lability of "zeolate" complexes[29,34] $(ZO)_2...WO_{2,3}...(NaOZ)_2$ relative to $(ZO)_2...MoO_{2,3}...(NaOZ)_2$. These observations suggest certain ideas about the mechanism[5] of the photooxidation reaction of $n[M(CO)_6]$–$Na_{56}Y$ in the presence of O_2.

Recall that α-cage encapsulated $W(CO)_6$ has two *trans*-carbonyl ligands anchored to site II Na^+ cations, namely, *trans*-$(ZONa)...(OC)W(CO)_4(CO)...(NaOZ)$.[5-7] Compared to "quasi gas phase" $W(CO)_6$ in solid Ar matrices, cation anchoring[5] appears to activate α-cage entrapped $W(CO)_6$ toward concerted oxidation of all six carbonyl ligands to CO_2. If by analogy with the work in solid Ar we hypothesize that the intermediate tungsten oxide product of the photolytic process in $Na_{56}Y$ is still monomeric WO_2, but anchored in the form $(ZO)_2...WO_2...(NaOZ)_2$ (as described earlier), then a subsequent photolytic or thermal step with O_2 could produce a less strongly anchored (partially freed) intermediate *cis*-$(O_2)WO_2...(NaOZ)_2$, which might be sufficiently mobile to participate in a bimolecular reaction with additional $(ZO)_2...$

(26) Lever, A. B. P. *Inorganic Electronic Spectroscopy*, 2nd Ed.; Elsevier Publ.: Amsterdam, 1984.

(27) Almond, M. J.; Downs, A. J. *J. Chem. Soc., Dalton Trans.* **1988**, 809.
(28) Roy, P. S.; Wieghardt, K. *Inorg. Chem.* **1987**, *26*, 1885.
(29) Özkar, S.; Ozin, G. A.; Prokopowicz, R. A. *Chem. Mater.* In press.
(30) Cotton, R. C.; Rabelais, J. W. *Inorg. Chem.* **1976**, *15*, 987.
(31) Fleisch, T. H.; Mains, G. J. *J. Chem. Phys.* **1982**, *76*, 780.
(32) Regalbuto, J. R.; Fleisch, T. H.; Wolf, E. *J. Catal.* **1987**, *107*, 114.
(33) Jaros, M. *Physics and Applications of Semiconductor Microstructures*; Oxford University Press: Oxford, 1989.
(34) Ozin, G. A.; Özkar, S. *Chem. Mater.* **1992**, *4*, 511.

$WO_2...(NaOZ)_2$ to yield the W_2O_6 dimer products $(ZONa)...O_2W(\mu\text{-}O)_2WO_2...(NaOZ)$. A similar type of reaction can therefore be envisaged for the "one step" thermal oxidation of $n[WO_2]$–$Na_{56}Y$ with O_2 at 300 °C to yield $n[WO_3]$–$Na_{56}Y$ (Figure 10).

The "two-step" vacuum thermal reduction of $n[WO_3]$–$Na_{56}Y$ to $n[WO_{2.5}]$–$Na_{56}Y$ and then to $n[WO_2]$–$Na_{56}Y$ is a much more difficult process to envision. The mechanism could be different for the low and high loading regimes. In the former case, both homo- and heterolytic $W(\mu\text{-}O)_2W$ bridge cleavage reactions of the W_2O_6 dimer are possible, leading to anchored WO_3 and WO_2 monomers (the former expected to be more labile than the latter), which could then participate in bimolecular encounters to yield W_2O_5 dimers, and then similarly on to anchored WO_2 monomers. In the latter case, bimolecular encounters between W_2O_6 dimers could result in O_2 loss from the $W^{6+}(\mu\text{-}O)_2W^{6+}$ bridge and formation of W_2O_5 dimers, a process which then repeats to yield WO_2 monomers. Spectroscopic and kinetic studies are underway, using extensive $^{12}C/^{13}C$ and $^{16}O/^{17}O/^{18}O$ isotopic labeling techniques, to quantitatively assess some of the mechanistic ideas discussed above.

Conclusions

A clean, mild, and quantitative photoinduced oxidative transformation of precursor $n[W(CO)_6]$–$Na_{56}Y$ in the presence of O_2 yields $n[WO_3]$–$Na_{56}Y$. Sequential saturation-filling photooxidation reactions allow one to essentially achieve full filling of $n \approx 32$ for the encapsulated WO_3 unit. Subsequent vacuum thermal treatments of $n[WO_3]$–$Na_{56}Y$ cause O_2 loss, which provides access to $n[WO_{3-x}]$–$Na_{56}Y$ materials in which one can systematically manipulate the oxygen content and structural and electronic properties of the imbibed WO_{3-x} guests over the entire composition field $0 < n \leq 32$ and $0 \leq x \leq 1$.

A multiprong approach to the structural characterization of these materials has revealed that well-defined monomeric, dimeric, and tetrameric molecular tungsten oxides WO_{3-x} exist in the α-cages of the $Na_{56}Y$ host for specific values of n and x: Na^+ cation anchored W_2O_6 dimers when $x = 0$ and $n = 16, 28, 32$; Na^+ cation anchored W_2O_5 dimers when $x = 0.5$ and $n = 16$; Na^+ cation anchored W_4O_{10} tetramers when $x = 0.5$ and $n = 32$; and Na^+ and oxygen framework anchored WO_2 monomers when $x = 1$ and $n = 16, 28, 32$.

Depending on the degree of filling of the α-cage void volume by these WO_{3-x} units, one can visualize them as either *isolated* or *coupled* within a molecular orbital or miniband[33] type description of their electronic properties.

For the special case of half- ($n = 16$) and full-filling ($n = 32$) of the "parent" $n[WO_3]$–$Na_{56}Y$, the available information suggests that these materials can be considered to be intrazeolite tungsten(VI) oxide supralattices, built up of α-cage W_2O_6 dimers at $n = 16$ and W_2O_6 *dimers-of-dimers* at $n = 32$. Intra- and intercavity coupling between W_2O_6 dimers provides one with a miniband type description of the electronic properties of these materials, Figures 12 and 13. In this view of the materials, one can consider that the thermal reductive-elimination of O_2 from $n[WO_3]$–$Na_{56}Y$ provides a simple chemical means of injecting variable numbers of electrons into an ordered array of electronically coupled W_2O_6 units. Thus one can precisely control the oxidation state, degree of n-doping, and extent of miniband filling of a tungsten(VI) oxide supralattice. This approach may prove valuable if these kinds of materials are ever to find application in catalysis, solid-state chemistry, and materials science.

Acknowledgment. We acknowledge the National Sciences and Engineering Research Council of Canada's Operating and Strategic Grants Programmes for generous financial support of this work. S.Ö. expresses his gratitude to the Middle East Technical University, Ankara, for granting him an extended leave of absence to conduct his research at the University of Toronto. Valuable discussion with and the assistance of Dr. Peter Macdonald (MAS-NMR), Mr. Raz Jelinek, Dr. Alex Pines (DOR-NMR), Dr. Heinz Robota, Dr. Karin Moller, Dr. Thomas Bein (EXAFS), Dr. Galen Stucky, Dr. W. Harrison (PXRD), Dr. Ross Davidson (XPS), and Dr. Neil Coombs (TEM, STEM-EDX) with various aspects of this project is most deeply appreciated. Research was carried out, in part, at the National Synchrotron Light Source, Brookhaven National Laboratory, Upton, NY, which is supported by the United States Department of Energy.

Metal–Metal vs Tellurium–Tellurium Bonding in WTe_2 and Its Ternary Variants $TaIrTe_4$ and $NbIrTe_4$

Arthur Mar, Stéphane Jobic,† and James A. Ibers*

Contribution from the Department of Chemistry and Science and Technology Center for Superconductivity, Northwestern University, Evanston, Illinois 60208-3113.
Received February 27, 1992

Abstract: The new ternary transition-metal tellurides $TaIrTe_4$ and $NbIrTe_4$ are ordered variants of the WTe_2 structure, which in turn is based on a distortion of the CdI_2-type layered structure. The layers in WTe_2 consist of buckled sheets of Te atoms, with the metal atoms residing in distorted octahedral sites. Through single-crystal X-ray diffraction methods, the structure of $TaIrTe_4$ has been determined and that of WTe_2 has been redetermined. The compounds $TaIrTe_4$ and WTe_2 belong to the space group C_{2v}^7-$Pmn2_1$ of the orthorhombic system with four formula units in cells of dimensions $a = 3.770$ (1), $b = 12.421$ (6), and $c = 13.184$ (6) Å and $a = 3.477$ (2), $b = 6.249$ (4), and $c = 14.018$ (9) Å, respectively, at 113 K. While metal–metal bonding is a structural feature common to all three compounds, Te–Te bonding is observed only in the ternary compounds. The trends of increasing metal–metal and decreasing Te–Te distances on progressing from WTe_2 to $TaIrTe_4$ and $NbIrTe_4$ have been rationalized by electronic band (extended Hückel) calculations. These trends are related to the creation of Te–Te bonds, ensuring the stability of the WTe_2 structure type even when addition of more d electrons leads to a weakening of metal–metal bonds. This concept is generalized to an entire series of compounds $MM'Te_4$ (M = Nb, Ta; M' = Ru, Os, Rh, Ir).

Introduction

In the past two decades, the synthetic chemistry of transition-metal chalcogenides has developed rapidly, primarily because these compounds are found to possess a rich structural chemistry[1] and a wide variety of unusual physical properties. These properties, associated with the anisotropic character inherent in these compounds, include charge density waves[2-9] and superconductivity.[10-14]

† Permanent address: Institut des Matériaux de Nantes, Laboratoire de Chimie des Solides, 2, rue de la Houssinière, 44072 Nantes, Cédex 03, France.

(1) *Crystallography and Crystal Chemistry of Materials with Layered Structures*; Lévy, F., Ed.; Physics and Chemistry of Materials with Layered Structures 2; D. Reidel: Dordrecht, Holland, 1976.

0002-7863/92/1514-8963$03.00/0